



Rational design of Ag/CuO@ZnIn₂S₄ S-scheme plasmonic photocatalyst for highly selective CO₂ conversion

Yining Zhang^{a,b,c}, Jinze Li^d, Weiqiang Zhou^a, Xin Liu^a, Xianghai Song^a, Songtao Chen^{b,c},
Huiqin Wang^{e,*}, Pengwei Huo^{a,*}

^a Institute of Green Chemistry and Chemical Technology, School of Chemistry & Chemical Engineering, Jiangsu University, Zhenjiang 212013, PR China

^b School of Ecology and Environment, Zhengzhou University, Zhengzhou 450001, PR China

^c College of Municipal and Environmental Engineering, Henan University of Urban Construction, Pingdingshan 467000, PR China

^d China Construction Power and Environment Engineering CO., LTD., Nanjing 210012, PR China

^e School of Energy and Power Engineering, Jiangsu University, Zhenjiang 212013, Jiangsu Province, PR China

ARTICLE INFO

Keywords:

Photocatalytic reduction of CO₂

Ag/CuO@ZnIn₂S₄

S-scheme heterojunction

Plasmonic effect

Covalent bonds

ABSTRACT

Designing S-scheme heterojunctions is an effective method to improve the charge localization on the surface of photocatalysts. Their effective charge transport routes can be enhanced with the help of interfacial noble metal nanoparticles. Herein, an Ag/CuO@ZnIn₂S₄ plasma S-scheme heterojunction with heterogeneous interfacial covalent bonds was successfully designed. The 15% Ag/CuO@ZnIn₂S₄ has promising photocatalytic performance and stability with the highest CO and CH₄ yields of 6.9 and 54.4 μmol g⁻¹ h⁻¹ and CH₄ selectivity of 92.8%. It is evidenced that the photogenerated charge can be efficiently separated and transported due to the influence of both the S-scheme electron migration mode and the Cu-S covalent bond. The process is further accelerated by using precious metals as cocatalysts, which can then selectively convert CO₂ into CH₄. This research is expected to provide helpful information for engineering S-scheme heterojunction photocatalysts and investigating their charge transfer kinetics.

1. Introduction

In the past decades, the intensified excessive use of carbon fuels has led to fossil energy depletion and a gigantic carbon footprint [1–3]. The conversion of anthropogenic CO₂ to fuels using renewable solar energy is a promising strategy to address the energy and environmental issues caused by CO₂ emissions [4–6]. Despite the considerable potential, the activation of CO₂ in carbonaceous fuels is among the formidable challenges due to linear carbon dioxide molecules with ultrahigh stability needing to absorb sufficient external energy to dissociate the C=O bond (750 kJ mol⁻¹) [7,8]. In the processes of producing single-carbon fuels, the formation of CH₄ is thermodynamically feasible in contrast to CO [9]. However, selective photosynthesis of CH₄ by the reduction process required transfer of eight electrons coupled with multiple protons is kinetically more hindering than that of CO by the 2e⁻/2 H⁺ reduction process, which mainly on account of the low light collection efficiency and the limited charge transport capacity of the photocatalyst [10–12]. Therefore, it is critical to design semiconductor catalysts with enhanced multielectron reduction capability.

As a new-arising and important ternary sulfide, ZnIn₂S₄ photocatalyst has been a favorite candidate for photoreduction CO₂, which can be attributed to its superior visible light absorption, appropriate energy band structure, sufficiently exposed reaction sites, excellent charge transport properties and nontoxicity [13,14]. Unfortunately, the photocatalytic performances of pure ZnIn₂S₄ still have room for further improvement, owing to surface charge localization and inferior charge transfer efficiency [15–17]. However, it is well known that the construction of heterojunction can help photogenerated electrons and holes obtain effective transfer and separation through the potential gradient formed between the heterogeneous interfaces to improve the photocatalytic performance of the catalytic materials.

Recently, one of the new S-scheme heterojunctions has become an important research field. This non-homogeneous structure promotes photogenerated carrier separation driven by its built-in electric field and still ensures the strong redox capacity of both semiconductor photocatalysts [18]. According to current reports, S-scheme heterojunction is composed of an oxidation photocatalyst (OP) and a reduction photocatalyst (RP) [19]. In S-scheme heterojunctions, a large number of

* Corresponding authors.

E-mail addresses: hqwang@ujs.edu.cn (H. Wang), huopw@ujs.edu.cn (P. Huo).

<https://doi.org/10.1016/j.apcatb.2023.123449>

Received 28 August 2023; Received in revised form 10 October 2023; Accepted 28 October 2023

Available online 30 October 2023

0926-3373/© 2023 Elsevier B.V. All rights reserved.

photogenerated electrons and holes are retained in the conduction band (CB) of the RP and the valence band (VB) of the OP, respectively, whereas, to retain the strong redox potential, the remaining nonsensical photoexcited carriers are recombined. Many semiconductor materials with suitable energy band positions can be combined with ZnIn_2S_4 to form this hierarchical heterostructure. As a typical example, Yu et al. [20] designed an S-scheme core-shell $\text{TiO}_2 @ \text{ZnIn}_2\text{S}_4$ heterojunction for photocatalytic CO_2 reduction. In this hybrid structure, ZnIn_2S_4 provides abundant reaction sites. At the same time, the S-scheme electron transfer structure can induce photogenerated carrier separation and transfer efficiently, thus significantly improving photocatalytic performance.

A typical transition metal oxide, CuO can be used as a suitable oxidation photocatalyst with a lower Fermi level [21,22]. Chen et al. [23] combined CuO with BiVO_4 (BVO) containing surface heterojunctions to construct a S-scheme system, which hindered charge recombination and promoted $\text{Cu}^{2+}/\text{Cu}^+$ cycling in the reaction, which had a positive effect on the photocatalytic process. Hitherto, the $\text{CuO} @ \text{ZnIn}_2\text{S}_4$ heterostructured interfaces have yet to be discussed. Hence, the vigorous construction between CuO and ZnIn_2S_4 and its facilitation of CO_2 photoreduction is worth investigating.

However, when exposed to a broad spectrum of light, most of the s-scheme heterojunctions produce an unequal charge distribution on the semiconductor components owing to differences in the bandgap of the constituent materials. To further solve the problem of charge separation, developing heterostructure contact interfaces with covalent bonding bonds is an attractive strategy [24]. These covalent bonds can act as a bridge for charge transfer and accelerate the vectorial migration of charges.

Significant studies have been devoted to the construction of S-scheme heterojunction catalytic systems with interfacial covalent bonds in the photocatalytic reaction of CO_2 reduction. Nevertheless, the design of materials capable of realizing selective conversion of CO_2 to CH_4 remains a challenge [25,26]. In view of the fact that the affluence of photogenerated charges is crucial for improving the product selectivity of CH_4 , the construction of multiple heterojunctions is considered a prospective strategy for accelerating electron transfer and enhancing the local electric field. Noble metal can be introduced into heterogeneous structures to generate local surface plasmon resonance (LSPR) effects as an additional energy input to improve photocatalytic activity [27]. For example, a $\text{Bi}_2\text{MoO}_6/\text{g-C}_3\text{N}_4$ S-scheme heterojunction was prepared by Shi et al. and loaded with Au as a co-catalyst further to accelerate carrier separation and transfer [28]. The composite catalysts exhibited excellent photocatalytic activity. The potential carrier transfer characteristics in this ternary hybrid and the reasons for increasing the CH_4 yield and selectivity are worthy of investigation.

Herein, we prepared a $\text{CuO} @ \text{ZnIn}_2\text{S}_4$ heterojunction by hydrothermal method. Ag NPs were introduced to modify the surface of the heterostructure by photodeposition, and an efficient $\text{Ag}/\text{CuO} @ \text{ZnIn}_2\text{S}_4$ ternary hybrid S-scheme heterojunction photocatalyst was successfully designed and applied to the photoreduction of CO_2 . The S-scheme charge transfer mechanism composed of CuO and ZnIn_2S_4 effectively promotes electron-hole separation while preserving the high redox capacity of the photocatalyst. Notably, the appearance of Cu-S covalent bonds in the composites also positively influenced both the separation of photogenerated charges and the reconstruction of the electronic arrangement of the reacting molecules. Moreover, Ag NPs further improve the photoelectric conversion efficiency of the hybrid material by using the LSPR effect and influence the product selectivity by controlling the reaction intermediate and the degree of CO_2 reduction [29]. This work provides a general approach to product selective tuning using metal cocatalysts in combination with S-scheme heterojunctions.

2. Experimental

2.1. Preparation of CuO nanorods

0.17 g $\text{CuCl}_2 \cdot 2\text{H}_2\text{O}$ was dissolved in 20 ml deionized water to form a translucent blue solution. Dissolve 0.16 g of NaOH in 40 ml of deionized water and drop slowly into aqueous CuCl_2 . Subsequently, keep stirring for 15 min. The mixture was transferred to a Teflonlined autoclave and reacted at 150 °C for 4 h. CuO nanosheets were obtained.

2.2. Preparation of $\text{CuO} @ \text{ZnIn}_2\text{S}_4$ composite materials

0.15 mmol ZnCl_2 , 0.3 mmol InCl_3 , 0.6 mmol Thioacetamide (TAA), and 1 mmol CuO powder were dissolved in 20 ml of ethylene glycol and stirred for 30 min to make a uniform mixture, then all the mixture was added in a Teflon tube and sealed in a stainless-steel autoclave. The autoclave was thereafter kept in an oven at 90 °C for 2 h, cooled naturally, and the precipitate was centrifuged and washed with deionized water and anhydrous ethanol. Then, it was dried overnight in a vacuum oven at 60 °C to obtain the 15%- $\text{CuO} @ \text{ZnIn}_2\text{S}_4$ (15-CZ). The $\text{ZnO} @ \text{ZIS}$ composite materials (denoted as x- $\text{ZnO} @ \text{ZIS}$, x = 5, 10, 20) at different mole ratios of ZnIn_2S_4 and ZnO were synthesized. The same method was used to synthesize the ZnIn_2S_4 monomer (ZIS) in the absence of ZnO.

2.3. Preparation of $\text{Ag}/\text{CuO} @ \text{ZnIn}_2\text{S}_4$ composite materials

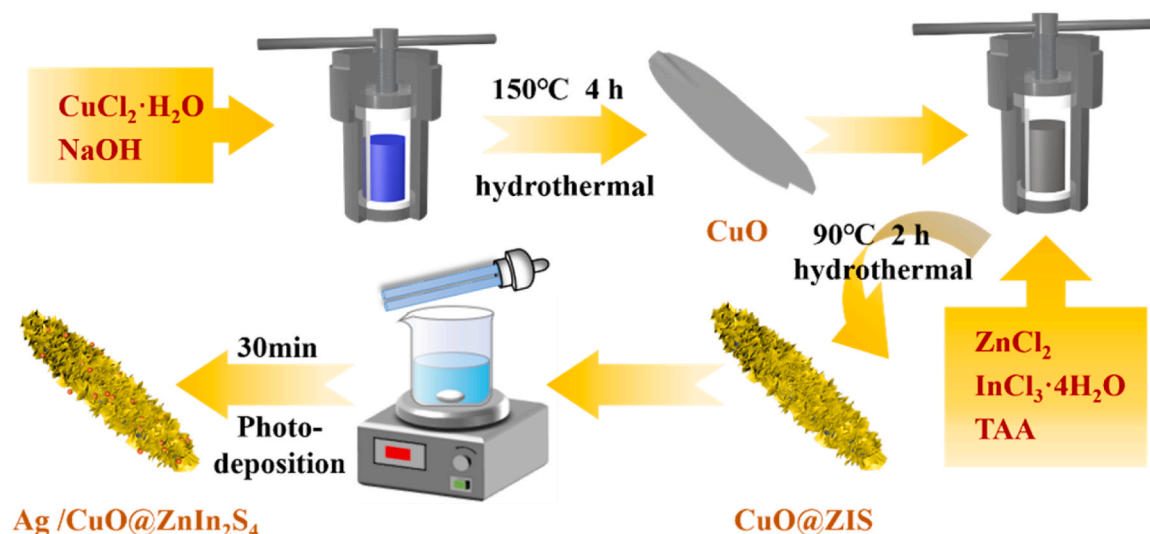
Dissolve 0.08 g of AgNO_3 in 10 ml of deionized water and stir well. Then, 0.1 g of 15-CZ was dispersed in a beaker containing deionized water for 5 min with ultrasonic dispersion, and 1 ml of AgNO_3 solution was added dropwise. Finally, the samples were repeatedly washed with water and ethanol and dried to obtain 15-CZ loaded with silver nanoparticles (Ag-NP), named 15- $\text{Ag}/\text{CuO} @ \text{ZnIn}_2\text{S}_4$ (15-ACZ). Meanwhile, 5-ACZ, 10-ACZ, and 20-ACZ were prepared according to the above method..

3. Results and discussion

3.1. Structure and morphology of catalysts

To investigate the crystalline phase and structure of obtained photocatalysts, XRD technology was performed and the patterns are shown in Fig. 1. For the pristine CuO, the characteristic peaks centered at 35.2°, 38.5°, 48.4°, 58.1°, 61.3°, 67.8°, and 74.8°, which indexed with (002), (111), (020), (202), (113), (022), and (004) lattice planes of CuO (PDF# 45-0973). Regarding ZIS, the diffraction peaks at 19.8, 27.4, 29.8, 47.3, 51.4, and 56.0°, matching well with the (006), (102), (104), (110), (116), and (022) crystal facets of hexagonal ZIS (PDF# 48-1778). Furthermore, all characteristic peaks can be assigned to CuO and ZIS in the patterns of 15-CZ and 15-ACZ composites. While, no typical diffraction peak of Ag was observed in the 15-ACZ characteristic peaks, which may be caused by the uniform dispersion and low abundance of Ag NPs [30]. Meanwhile, a slight increase in the intensity of the diffraction peaks centered at 22.2° and 28.5° as a consequence of Ag NPs. This is probably on account of deformation in the ZIS sheet structure as a consequence of the application of Ag NPs [31]. Moreover, Raman spectroscopy verified the successful fabrication of the composites (Fig. 2b). Interestingly, in addition to the signal peaks of two monomers, the binary hybrid material and the ternary hybrid material also obtained a new characteristic peak situated at 123 cm^{-1} . The new emerging peak can be indexed to the Cu-S bonding state, suggesting that the ZIS and CuO were combined intimately by the Cu-S bond. These results reflect the coexistence of CuO, ZIS, and Ag NPs, which preliminarily confirms the successful hybridization of 15-ACZ heterojunction photocatalyst.

The morphology of samples was characterized by scanning electron microscopy (SEM) and transmission electron microscopy (TEM). Fig. 2c



Scheme 1. Schematic diagram of the preparation of 15-ACZ.

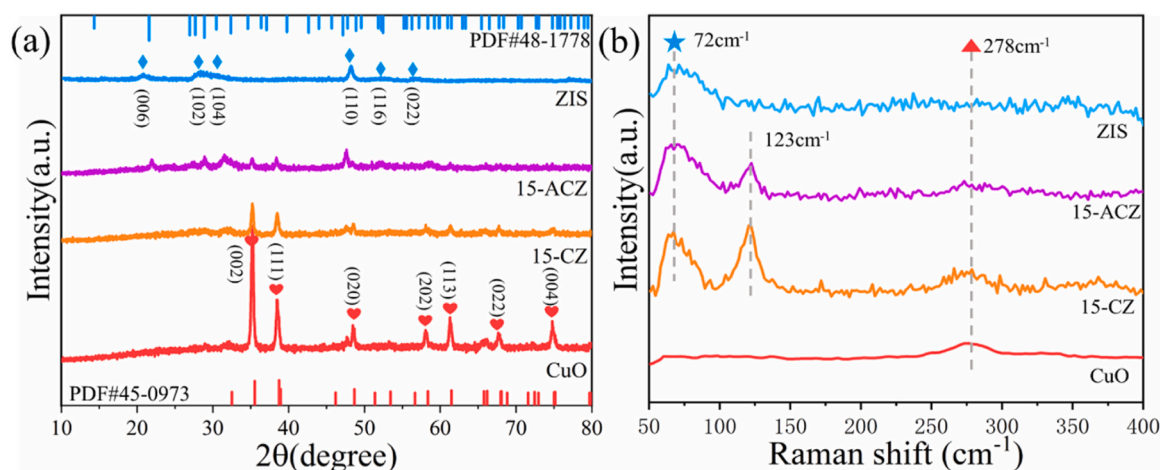


Fig. 1. (a) XRD patterns and (b) Raman spectra of CuO, ZIS, 15-CZ, and 15-ACZ composite photocatalysts.

shows that the prepared CuO presents a regular blade shape with a smooth surface. The original ZIS, by contrast, was a flower-like microsphere architecture made up of nanosheets. Fig. 2a shows the morphologies of 15-ACZ composites, a large number of the ZIS nanosheets in situ grow densely until they are completely and uniformly covering the surface of CuO nanosheets. SEM images of CuO monomer and binary composite are shown in Fig. S1. The TEM image (Fig. 2b, c) confirms that CuO and ZIS are thin sheet materials intimately integrated after hydrothermal treatment. In addition, the morphology of Ag NPs composite samples did not change significantly after photodeposition (Fig. 2e). The effective combination of CuO, ZIS, and Ag NPs is exhibited in the high-resolution transmission electron microscopy (HRTEM) image, where the lattice spacings be measured to be 0.25 and 0.32 nm are well corresponding to (002) of CuO and (102) of ZIS, and 0.192 nm interplanar spacings can be assignable to the (002) plane of Ag (Fig. 2f). The energy-dispersive X-ray spectroscopy (EDS) elemental mapping images (Fig. g-m) of the 15-ACZ reveal the uniform distribution of Cu, O, Zn, In, and S elements, and the results are consistent with XRD results. Additionally, in order to further validate the actual composition of CuO, ZIS, and Ag in the sample, an inductively coupled plasma (ICP) test was conducted to determine the specific proportion of metal elements in the 15-ACZ ternary hybrid sample. The concentrations of Cu, Zn, In, and Ag in the samples were 33.75%, 5.68%, 12.38%, and 0.76%, respectively,

which further proves the successful fabrication of a 15-ACZ heterogeneous composite.

Nitrogen adsorption isotherms for the characterization of gas adsorption on the photocatalyst surface (Fig. 3). ZIS had characteristic IV-type isotherms and H3-type hysteresis loops, while all other samples showed III-type isotherms (Fig. 3a) [32]. In addition, the N_2 physorption data for all catalysts can be referred to in Table S1 in the support information. Evidently, as the mass fraction of ZIS in the composites increased, their specific surface area also increased gradually. It is worth noting that the specific surface area of 15-ACZ showed a decreasing trend after the deposition of Ag NPs, which may be attributed to the blocking of some pore structures in the photodeposition process. However, the decrease in the specific surface area of 20-ACZ can be attributed to the agglomeration of ZIS on the CuO surface due to excessive loading. Additionally, the pore size distribution conforms to that of small mesopores or micropores. The bigger specific surface area of 15-ACZ may provide more adsorption sites and surface activity, which benefit photocatalytic processes [33]. The CO_2 adsorption and desorption curves can directly reflect the CO_2 adsorption capacity of the prepared sample. The CO_2 adsorption capacity basically increased linearly with the increase of absolute pressure in the whole P/P_0 range, certifying that CO_2 mainly existed on the catalyst surface through physical adsorption (Fig. 3b) [34]. In addition, the CO_2 desorption curve shows

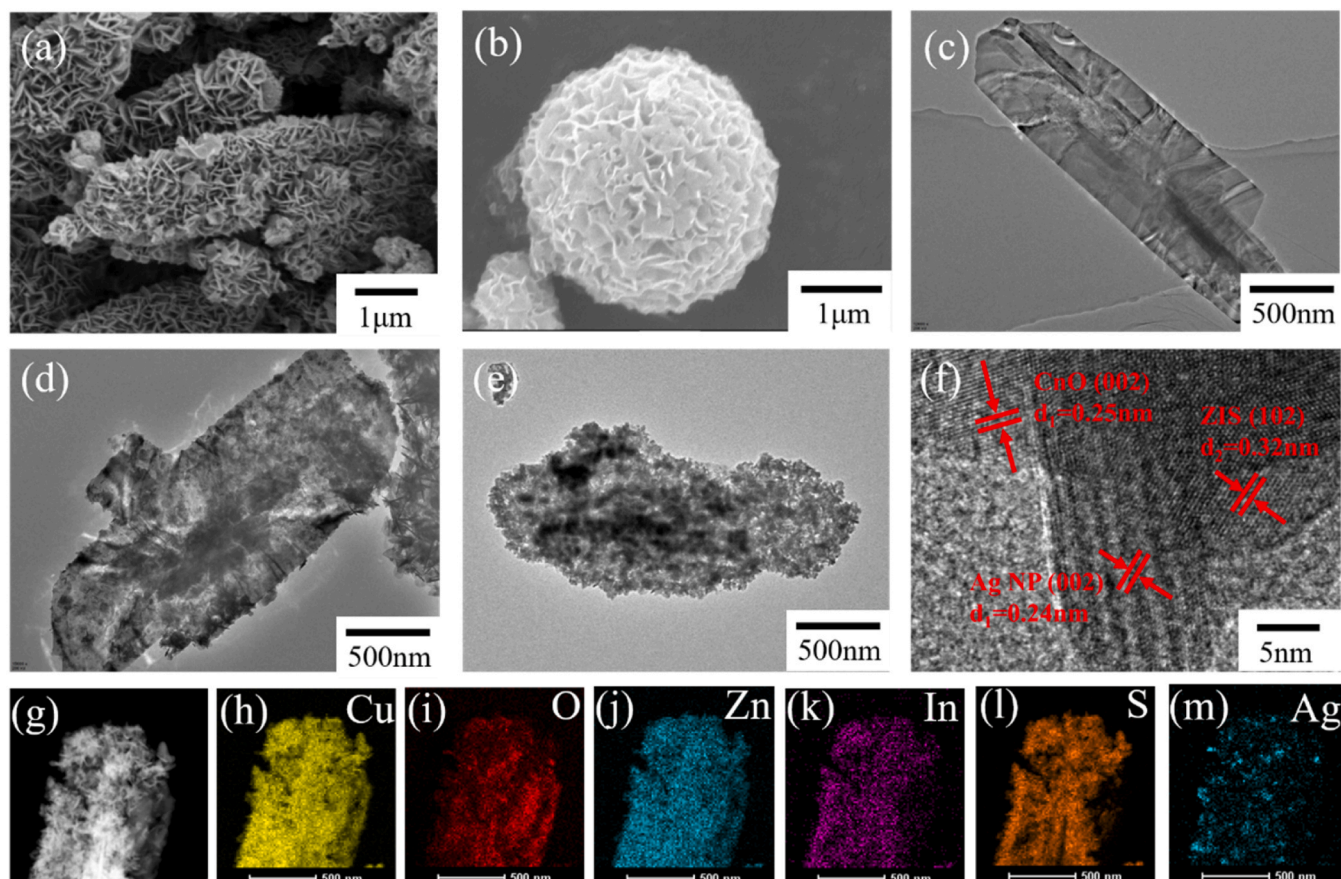


Fig. 2. SEM images of (a)15-ACZ, (b) ZIS; TEM results of (c) CuO, (d)15-CZ,(e) 15-ACZ; (f) HRTEM image of 15-ACZ. (g-m) Elemental mapping of 15-ACZ.

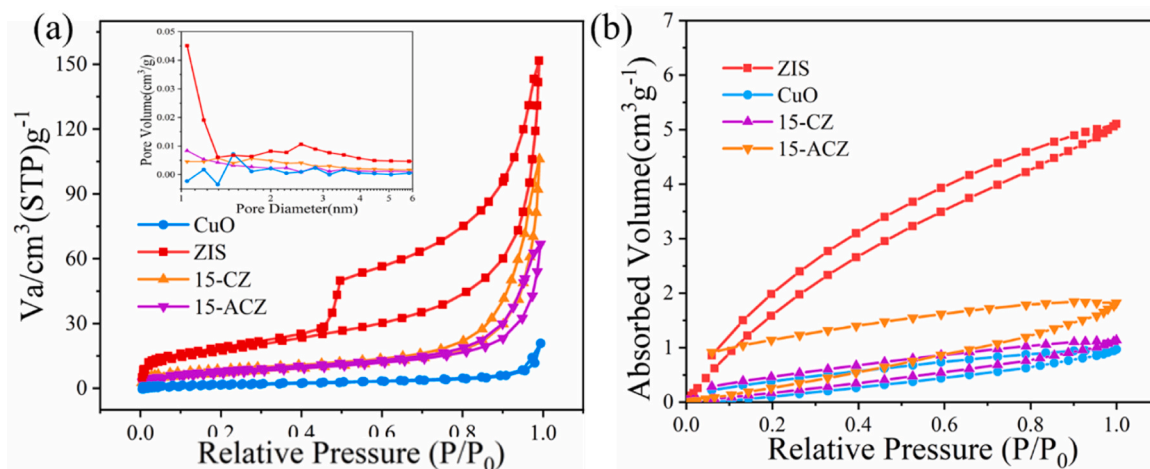


Fig. 3. (a) N_2 adsorption-desorption isotherms and pore size distribution of CuO, ZIS, 15-CA, and 15-ACZ; (b) CO_2 adsorption and desorption curves of CuO, ZIS, 15-CA, and 15-ACZ.

that the pressure required for desorption is much lower than that for adsorption. In the process of adsorption capacity and desorption, the large pressure hysteresis phenomenon indicates that there is a strong interaction between adsorbent and adsorbent [35]. It is evident that the CO_2 adsorption capacity of the catalyst is positively correlated with its S_{BET} . The results are consistent with the characterization of photocatalyst properties.

3.2. Surface chemical state

X-ray photoelectron spectroscopy (XPS) was used to assess the surface chemical states of the samples. Fig. 4a revealed the Zn 2p spectra with two characteristic peaks appearing at 1021.9 eV and 1044.9 eV, corresponding to Zn 2p_{3/2} and Zn 2p_{1/2}, respectively. Fig. 4b revealed that the characteristic peaks centered at 445.2 and 452.8 eV can be assigned to In 3d_{5/2} and In 3d_{3/2} orbitals, indicating a valence state of +3 [36]. Fig. 4c presents characteristic peaks of the S 2p in ZIS at binding energies of 161.7 eV and 162.9 eV, which could be attributed to the S

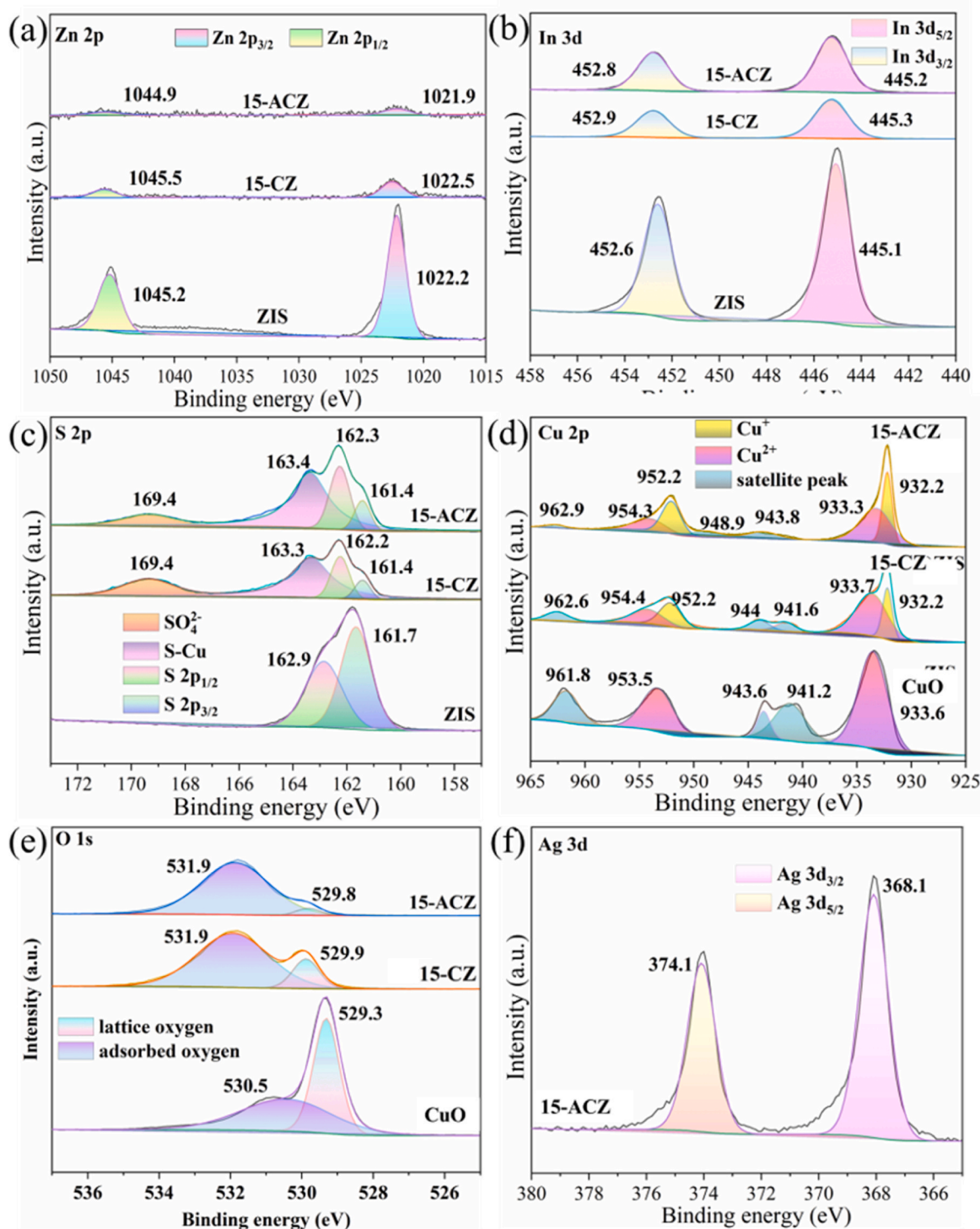


Fig. 4. XPS spectra of CuO, ZIS and 15-ACZ: (a) Zn 2p, (b) In 3d, (c) S 2p, (d) Cu 2p, (e) O 1s, (f) Ag 3d.

$2p_{3/2}$ and $S 2p_{1/2}$ of S^{2-} ions in 15-CZ and 15-ACZ [37]. The new characteristic peaks at 163.3 eV and 169.4 eV appeared when ZIS was in situ coated with CuO, in $S 2p$ spectra can be assigned to the Cu-S bond and sulfate group [15]. The formation of Cu-S bonds further demonstrates a strong interaction between the two original materials, which can establish an efficient electron transfer mode to rearrange electrons from the O or C of CO_2 adsorbed on the catalyst for the activation of CO_2 molecules [38]. Additionally, the SO_4^{2-} ions can reduce the OER overpotential and promote surface carrier transfer by breaking the adsorption-energy scalar relationship between OH^* and OOH^* reaction

intermediates, thus enhancing the redox ability of the material [39]. Apparently, Cu 2p could be resolved into five peaks in the spectrum of CuO (Fig. 4d). Thereinto, the peaks at 933.6 eV and 953.5 eV denote Cu $2p_{3/2}$ and Cu $2p_{1/2}$, respectively, while the peaks at 941.2 eV, 943.6 eV, and 961.8 eV are the satellite peaks of Cu^{2+} [40,41]. After incorporating the ZIS material, the valence state of copper changed and the peaks of Cu^+ ions started to appear. This may be due to the reduction of Cu^{2+} by the TAA added during vulcanization. Cu^+ possesses higher thermal stability because it is the d^{10} conformation located closer to the VB of the host and has a more minor Stokes shift. The characteristic peaks of O

appearing at binding energies of 529.3 eV and 530.5 eV could be ascribed to lattice oxygen and adsorbed oxygen (Fig. 4e). Of these, adsorbed oxygen is an essential active substance in the process of photoreduction of CO₂ [42]. The proportion of adsorbed oxygen in the spectra of binary and terpolymer hybrid materials is increased, which is more favorable for the catalyst to participate in the photoreduction process. Fig. 4f shows the two binding energies located at 368.1 eV (Ag 3d_{3/2}) and 374.1 eV (Ag 3d_{5/2}), which should be attributed to the presence of Ag⁰. The above results point to the successful deposition of Ag monomers. In addition, it can be observed that the characteristic peaks representing Zn and In in the image move towards the direction of

high binding energy, while the characteristic peaks belonging to Cu and O move towards lower binding energy. It is well known that changes in binding energy are closely related to electron density [43]. Therefore, it is concluded that the electron cloud density of ZIS decreases at the composite interface, whereas the electron cloud density of CuO increases. This benign electron transfer is consistent with an S-scheme mechanism [44].

3.3. Optical absorption properties and energy band structure

The UV–Vis diffuse reflectance spectra (DRS) of ZIS, CuO, 15-CZ, and

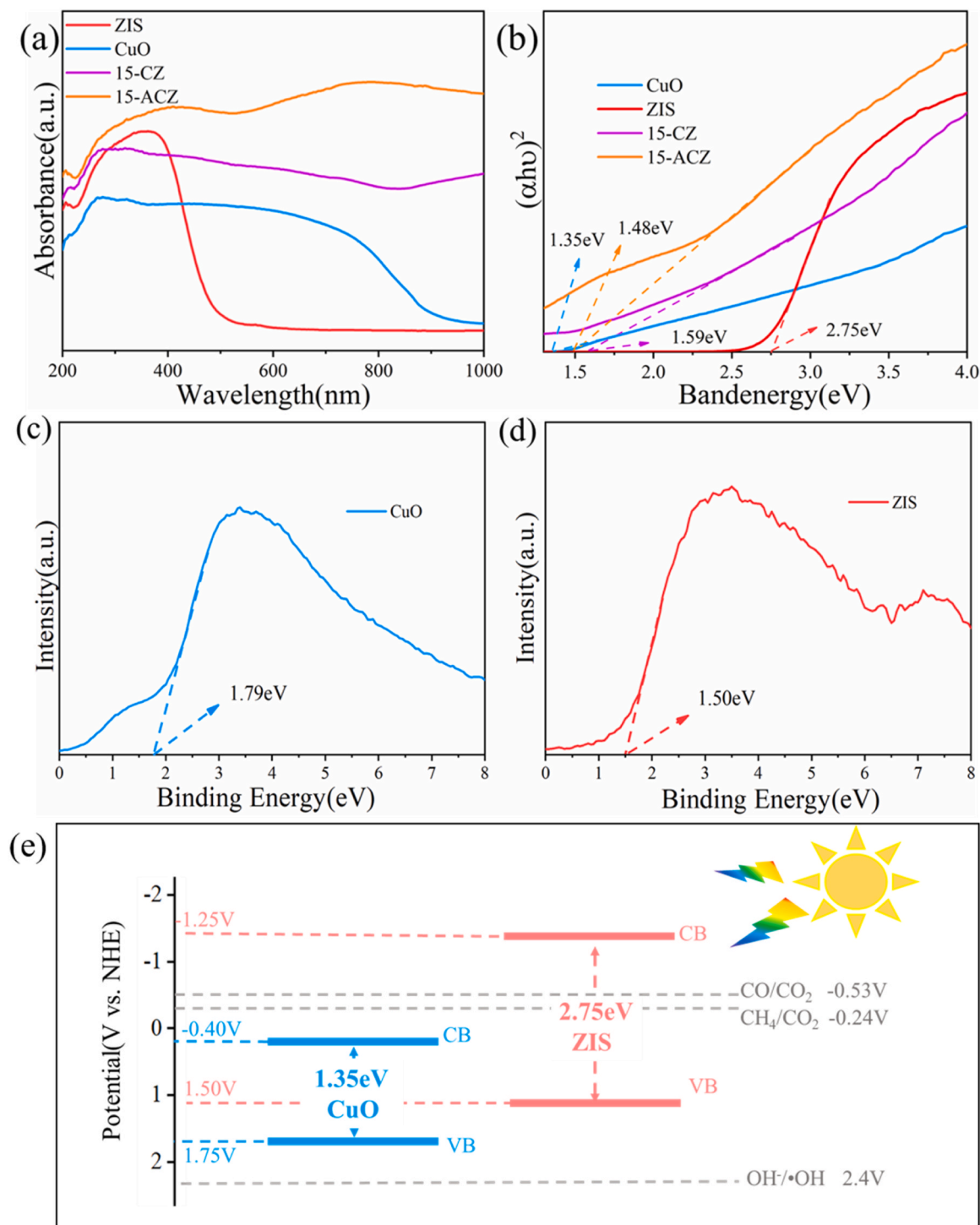


Fig. 5. (a) UV–Vis DRS and (b) the Tauc plots of ZIS, CuO, 15-CZ and 15-ACZ. VB-XPS spectra of (c) ZIS and (d) CuO. (e) Energy band structures of ZIS and CuO.

15-ACZ, characterize the optical absorption characteristics of the photocatalyst (Fig. 5a). Apparently, the ZIS sample exhibits an intense absorbance signal in the UV region. However, CuO containing samples had good absorption, which can be attributed to the black nature of itself [45,46]. At about 420 nm, the visible light absorption of 15-ACZ is markedly enhanced, which can be attributed to the LSPR of Ag NPs [26]. As shown in Fig. 5b, the band gap values of each sample were calculated by fitting the UV-vis data with the following formula:

$$(\alpha h\nu)^{\frac{1}{n}} = A(h\nu - E_g)$$

where α , $h\nu$, and E_g are respectively absorbance coefficient, incident photon energy and bandgap energy. When $n = 1/2$, the formula applies to semiconductor materials with a direct band gap. In this case, n is equal to $1/2$ [47,48]. It can be seen that after incorporation of CuO with a narrower band gap (1.35 eV), the band gap of the binary composite becomes 1.59 eV, which is narrower than that of ZIS (2.75 eV) (Fig. 5c, d). Besides, the LSPR effect of Ag will further affect the band gap of the composite catalyst while enhancing light absorption [49], which means that Ag NPs can regulate the selectivity of the product by changing the band structure. The band structures of ZIS and CuO are shown in Fig. 5e. The 15-ACZ ternary hybrid can be photoexcited again at 420 nm to further enhance its light absorption, which facilitates the photogenerated carrier production and the enhancement of the catalyst photoreduction ability.

To further investigate the plausible mechanism, the electron spin resonance (ESR) measurements are used to analyze free radicals during photoreduction after they were captured by 5,5-dimethyl-1-pyrroline-Noxide (DMPO) agents (Fig. 6). For the ZIS, CuO, and 15-ACZ, no ESR signal was observed in the dark. Compared with monomeric materials, the 15-ACZ has significantly stronger ESR signals for both $\text{DMPO}\cdot\text{O}_2^{\cdot-}$ and $\text{DMPO}\cdot\text{OH}$ under illumination, which provides strong evidence for its strong REDOX ability. In addition, as shown in Fig. 6a, the hole potential in VB of CuO makes it easier to efficiently oxidize OH to $\cdot\text{OH}$, while the electrons in CB have difficulty in reducing O_2 to $\cdot\text{O}_2^{\cdot-}$. The ESR peak results of ZIS show the opposite (Fig. 6b). Therefore, ESR results can demonstrate that photoinduced electrons and holes are retained in the CB of ZIS and the VB of CuO, respectively, and that the photo-induced charge transfer mechanism between ZIS and CuO would follow the unique S-scheme mechanism rather than the conventional type-II heterojunction mechanism [50,51]. This is consistent with the results of XPS patterns and energy bandgap structures of the material.

3.4. Photoelectrochemical properties analysis

The separation characteristics of electron-hole pairs are examined by PL and TR-PL spectra (Fig. 7a, b). After integrating CuO and Ag NPs, the PL intensities obviously drop, implying that the recombination of photogenerated electron-holes can be availably restrained by the 15-ACZ heterojunction [52,53]. In addition, the TRPL is employed to further probe the migration behavior of charges. Obviously, the 15-ACZ has a shorter average decay lifetime (0.40 ns) than that of bare CuO (0.65 ns) and 15-CZ (0.45 ns), reflecting an excellent capacity of 15-ACZ for charge separation and transfer [54]. As shown in Fig. 7c, to further examine charge transfer, the transient photocurrent response (TPR) of different catalysts under intermittent light irradiation was measured [55]. It can be seen that all catalysts have relatively stable photocurrent densities, with the most vital photocurrent signals for the ternary hybrid and increased photocurrent density intensity for the binary complexes compared to bare CuO and ZIS, which proves that the S-scheme heterostructure is more favorable for photogenerated electron-hole separation [56]. In combination, CuO and ZIS interfacial covalent bonding interactions accelerate the vectorial migration of photogenerated charges, while the S-scheme charge transport mode guarantees the charge separation efficiency. Additionally, the presence of multiple charge transfer in the hybridization after the introduction of Ag NPs can further increase the photoexcited electron consumption. The electrochemical impedance spectroscopy (EIS) spectra of ZIS, CuO, 15-CZ, and 15-ACZ are shown in Fig. 7d. Of these, 15-ACZ has the smallest EIS Nyquist radius and therefore the lowest charge transfer resistance. In other words, the composites have relatively superior charge transfer properties [57]. Consequently, 15-ACZ displayed the optimal photocatalytic CO_2 reduction activity.

3.5. Photocatalytic performance

The performance of the synthesized catalyst for CO_2 reduction was examined under 300 W xenon lamp irradiation without the use of photosensitizer or sacrificial agent. Fig. 8a demonstrates that ZIS and CuO can only produce CO with the poor activity of $0.8 \mu\text{mol g}^{-1} \text{h}^{-1}$ and $2.4 \mu\text{mol g}^{-1} \text{h}^{-1}$. After the two monomer materials are combined, the CO yield of the optimum composite sample increased by nearly 4.8 times to $11.6 \mu\text{mol g}^{-1} \text{h}^{-1}$ compared with the original CuO, explaining that the construction of S-scheme heterojunction and Cu-O bond plays a critical influence on the photocatalytic performance. Although the yield of CO is increased, other products containing element C were not detected, which can be attributed to the fact that the charge transfer efficiency of 15-CA is still limited in providing enough electrons and

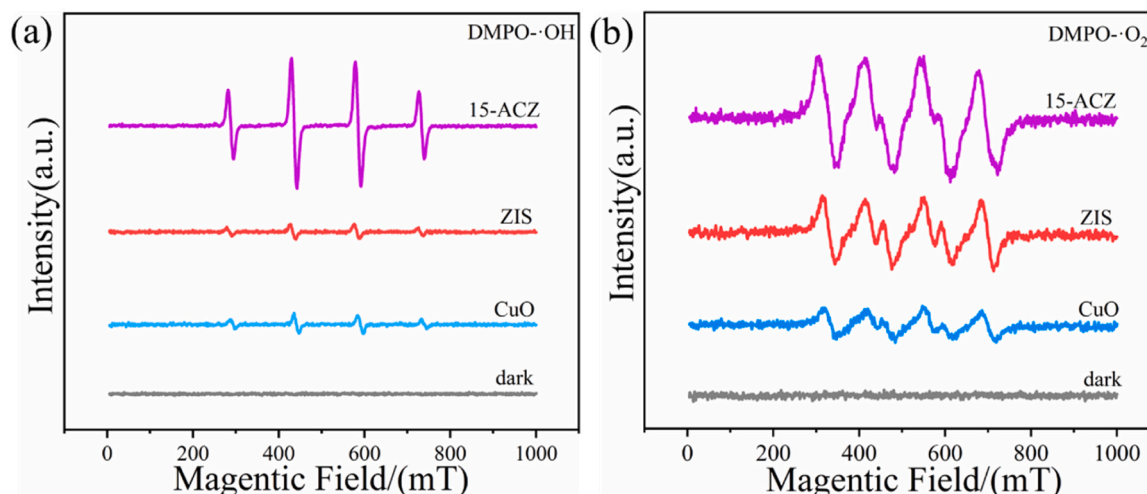


Fig. 6. (a) $\text{DMPO}\cdot\text{OH}^{\cdot}$ and (b) $\text{DMPO}\cdot\text{O}_2^{\cdot-}$ for CuO, ZIS, and 15-ACZ.

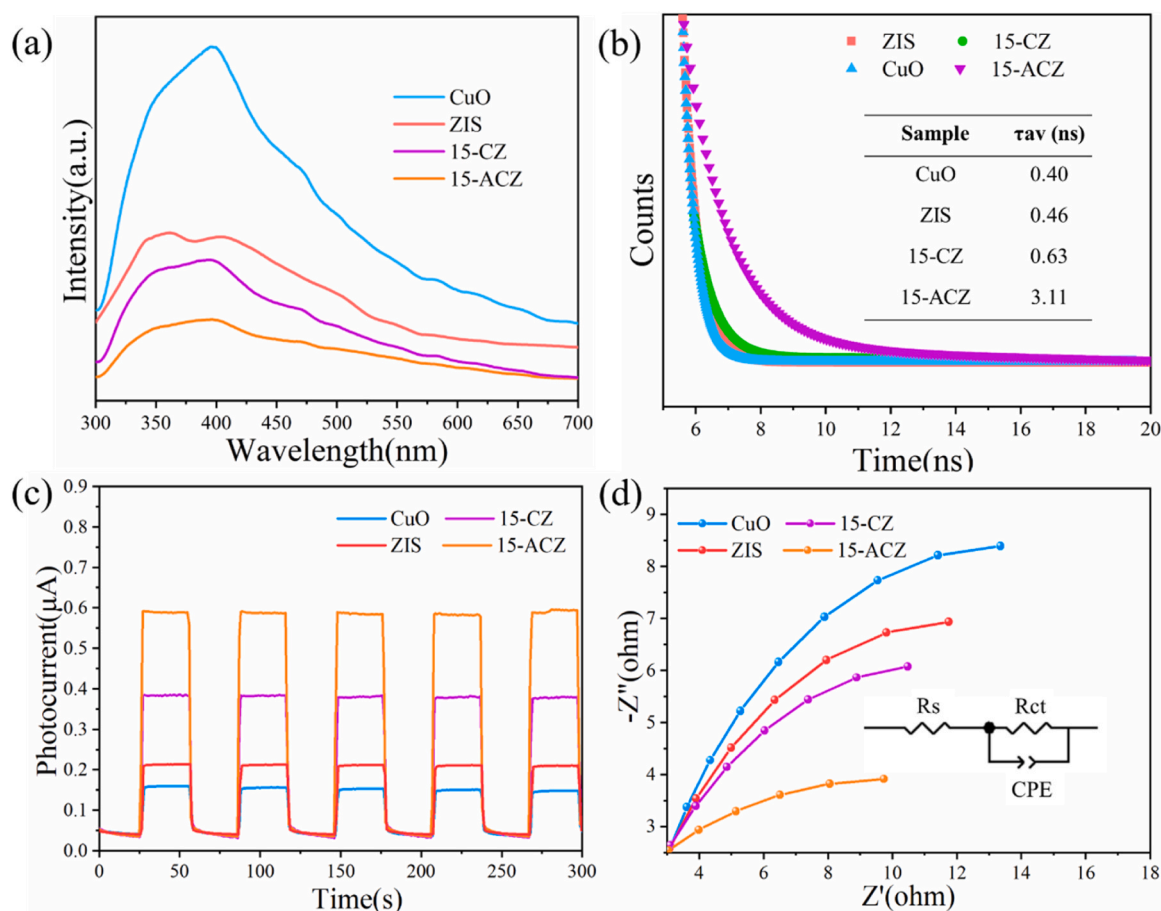


Fig. 7. (a) PL and (b) TR-PL decay spectra of the CuO, ZIS, and 15-ACZ samples (c) TPR (d) EIS spectra of the CuO, ZIS, 15-CZ, and 15-ACZ samples.

protons to yield CH_4 . After introducing Ag NPs, the CO production ($16.9 \mu mol g^{-1} h^{-1}$) rates were further improved and could have up to 92.8% selectivity for light-driven CO_2 reduction into CH_4 ($54.4 \mu mol g^{-1} h^{-1}$) (Fig. 8b), which establishes that Ag NPs function as photogenerated electron-rich sites, increasing the electron-proton density under vectorial multistep charge transfer throughout the catalytic system and rendering the catalysts more inclined to form CH_4 products [58]. The CO_2 reduction ability of the ternary hybrid material increases with the increase of the mass fraction of ZIS, but the photocatalytic performance of the material decreases with excessive ZIS. This may be owing to the decrease in the specific surface area of the catalyst due to the introduction of excess ZIS, which reduces the adsorption capacity for CO_2 . The effect of Ag co-catalyst loading on photocatalytic CO_2 reduction in 15-ACZ hybrids was then investigated. As shown in Fig. 8c, the CH_4 productivity increased with increasing Ag loading and reached the highest CH_4 productivity at an Ag loading of 8 wt%. It is evident that a decrease in the rate and selectivity of CH_4 production occurs when Ag is overloaded, which can be attributed to the fact that excess Ag agglomerates on the surface of the binary catalyst and becomes an electron-hole complex center. In addition, as the loaded Ag content increases, the distance between the holes on ZIS and the electrons on Ag may become shorter, increasing the chance of electron and hole complexation. More practically, the 15-ACZ catalyst exhibited excellent cycling performance. One cycle of testing was conducted every 4 h for a total of 4 cycles, during which the CH_4 production rate remained essentially stable (Fig. 8d). To visualize the high electronic excitation efficiency of the catalysts under irradiation, quantum efficiency (QE) calculations at different wavelengths were carried out (Fig. S2). Apparently, the catalyst achieved a higher QE at 420 nm, which further demonstrated that Ag as a co-catalyst helped the heterogeneous system to better capture

the incident light to generate high-energy hot electrons [59]. A comparison of the photocatalytic activity with reported similar catalysts can be seen in Table S2. Furthermore, the XRD images (Fig. S3) before and after the reaction showed no obvious changes in the structure and crystalline phase of the catalyst, which proved that the catalyst had a low degree of photocorrosion and excellent stability during the reaction process.

3.6. Photocatalytic CO_2 reduction mechanism

In situ, FTIR was carried out to probe the reaction mechanism, especially the promoting effect of Ag for CH_4 selectivity by reaction intermediate species. Fig. 9 shows the dynamic changes of the carbon-based groups on the prepared sample surface within 0–20 min of illumination. Firstly, the monodentate carbonate ($m-CO_3^{2-}$, 1401, 1426, 1368 and 1348 cm^{-1}), and bidentate carbonate ($b-CO_3^{2-}$, 1468, 1351, 1330, 1328 and 1315 cm^{-1}) indicated that CO_2 and H_2O molecules adsorption activation on the surface of the sample (Fig. 9a–f). IR peaks representing the vibrations of $COOH^*$ groups were observed in ZIS, CuO, 15-CZ, and 15-ACZ, which is one of the critical intermediates in the photoreduction of CO_2 to $C1$ [60]. It is noteworthy that the intensity of the absorption bands representing the CH_3O^* group at 1037 and 1183 cm^{-1} visibly increased with the accumulation of irradiation time, while the characteristic peak of the CHO^* group was located at 1128 cm^{-1} (Fig. 9g, h) [61]. This confirmed that the presence of Ag NPs can generate more hot electrons and help the $COOH^*$ groups adsorbed on the catalyst surface to accept electrons to form CHO^* and CH_3O^* -intermediate groups, which proved to be essential intermediates for CH_4 products. Therefore, it can be considered that format species was photoreduced to CH_4 on 15-ACZ, which could be attributed to Ag NPs on

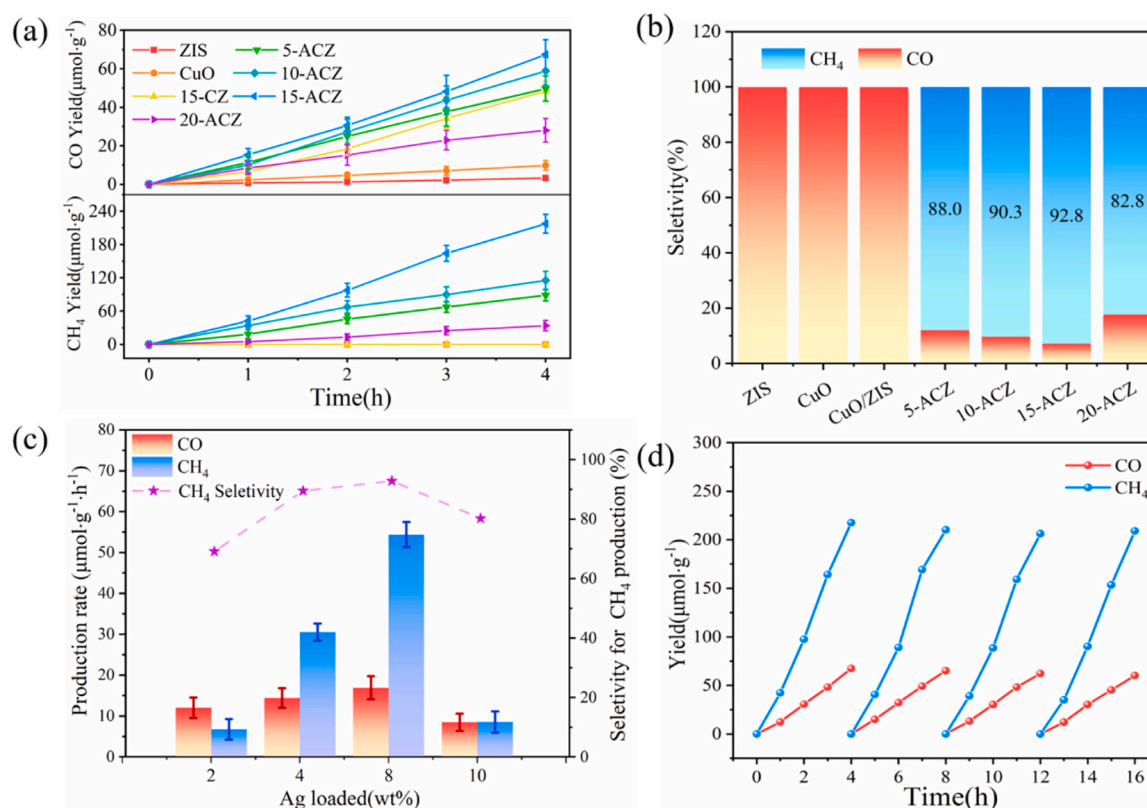


Fig. 8. (a) Photocatalytic activity and (b) selectivity of CH₄ of CuO, ZIS, 15-CZ, and 15-ACZ; (c) production rates and the selectivity of CH₄ by different Ag loading contents of ACZ; (d) cycling tests.

the catalyst surface promoting the adsorption and conversion of format [62]. In addition, the infrared characteristic peak of COOH* is extremely weak compared to that before the introduction of Ag NPs, which indicates that the 15-ACZ composite sample has a high selectivity to CH₄.

We simulated the charge density difference of the ACZ composite sample. The charge density difference distribution of the ACZ is shown in the inset of Fig. 10. The yellow area represents electron aggregation, and the blue area exhibits electron exhaustion. This demonstrates that the CuO and ZIS have intense interactions and charge transfer [63]. At the interface of the CZ heterogeneous structure, the surface of CuO is mainly covered by yellow, and a small amount of blue area. While, the surface of ZIS is primarily green. The electron density difference along the binding z direction (Fig. 10e) more clearly shows the direction of electron flow between interfaces. As a result, electrons are transferred from pure ZIS to CuO in the heterojunction and create an internal electric field (IEF), which is consistent with the band structure analysis described above. The simulation results demonstrate that the IEF and the interfacial charge redistribution induced by the Cu-S covalent bond energy at the heterogeneous interface, which is in accordance with the results of XPS spectroscopy and energy-low structure analysis.

The localized electric field enhancement and the LSPR of 15-ACZ under light excitation of 420 nm were simulated by the finite difference time domain method (FDTD) simulation method. The cross-section models of 15-CZ and 15-ACZ were simplified to facilitate the simulation of electric field strengths (Fig. 10f, g). Fig. 10f shows that 15-CZ exhibits a weak field intensity at the interface when excited at 420 nm, generated by a photoexcited semiconductor. Significantly, the local electromagnetic field density near the Ag at the ternary interface is improved and the plasmonic "hot spot" [64], can be observed in the nanoscale gaps between Ag nanoparticles and ZIS nanosheets, which indicates that a large amount of charge has accumulated at the interface (Fig. 10g). The above simulation results show that after Ag excitation, the LSPR effect can effectively promote the high-speed hot electron transfer across the

semiconductor heterogeneous interface to inhibit the fast relaxation of hot electrons, thereby increasing the overall concentration of charges in the heterojunction and finally improving its catalytic activity [65,66]. This is consistent with the results of UV-Vis DRS characterization and performance tests.

3.7. Photocatalytic mechanism

A possible photocatalytic reaction mechanism for photoproducted CO₂ over Ag/CuO@ZnIn₂S₄ was tentatively proposed according to the results mentioned above. Considering the variation of the electronic binding energies of the elements, the energy band alignments, and the free radical generation results, a hypothetical S-scheme charge transfer pathway is proposed. As can be seen from Fig. 11, the monomer ZIS has a high Fermi level. When a CuO@ZnIn₂S₄ heterojunction is established, electrons flow freely from ZIS to CuO until the Fermi level stabilizes at the interface. On the other hand, the migration of electrons at the heterogeneous interface also results in a downward bending of the energy band of CuO, forming an electron aggregation region at the interface, whereas an upward bending of the energy band of ZIS, forming an electron dissipation region at the interface [67,68]. In this case, an IEF is formed by the directional movement of electrons between the two interfaces. In addition, Cu-S chemical bonding provides fast charge transfer channels exposed to strong IEF, enabling interfacial electron redistribution. At the same time, Cu-S bond significantly accelerates S-scheme charge transfer and enabling efficient space charge separation [69]. When the hybridized structure is excited under light, photo-generated electrons and holes in the redox process are better separated and transferred to CB of ZIS and VB of CuO. In addition, Ag NPs serve as active reaction sites and efficient electron transport receptors. As exceptional electron traps, they facilitate enhanced transfer of photo-generated electrons and more effective separation of electron holes. More importantly, the LSPR effect of Ag NPs can promote light

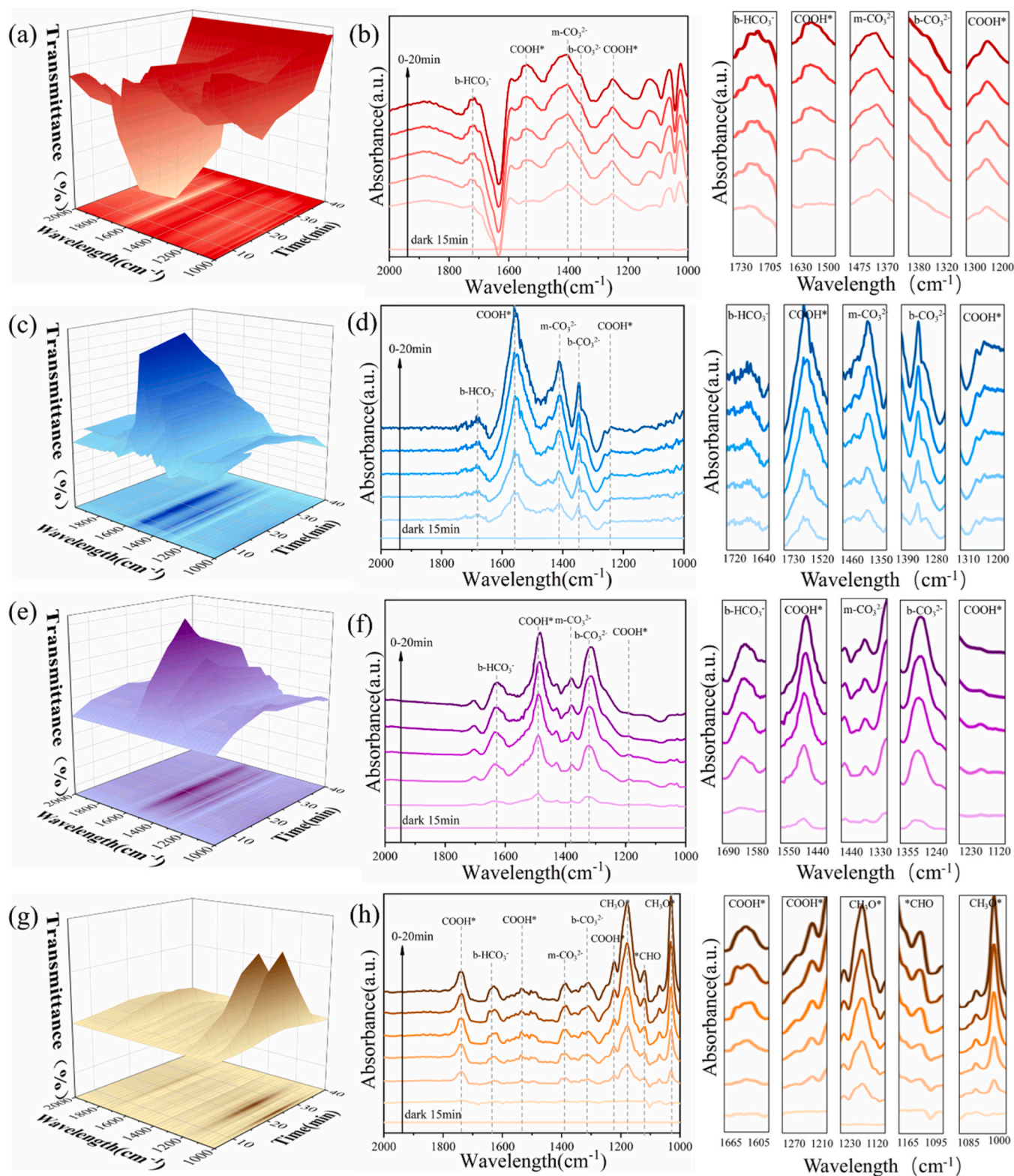


Fig. 9. The 3D color-mapped surface map with projection (a, c, e, g); *In situ* FT-IR spectra of CO₂ reduction process on (b) ZIS, (d) CuO, (f) 15-CZ, and (h) 15-ACZ composite under the illumination process.

absorption and provide more hot electrons for the process of reducing CO₂ to CH₄, increasing the overall charge concentration in the heterojunction, which is critical to the increasing CH₄ conversion rate and selectivity.

4. Conclusions

In summary, a plasmonic S-scheme heterojunction Ag/CuO@ZnIn₂S₄ photocatalysts were successfully fabricated via a hydrothermal method and photodeposition method and were applied on high-efficiency photoconversion of CO₂ into CH₄. The main products

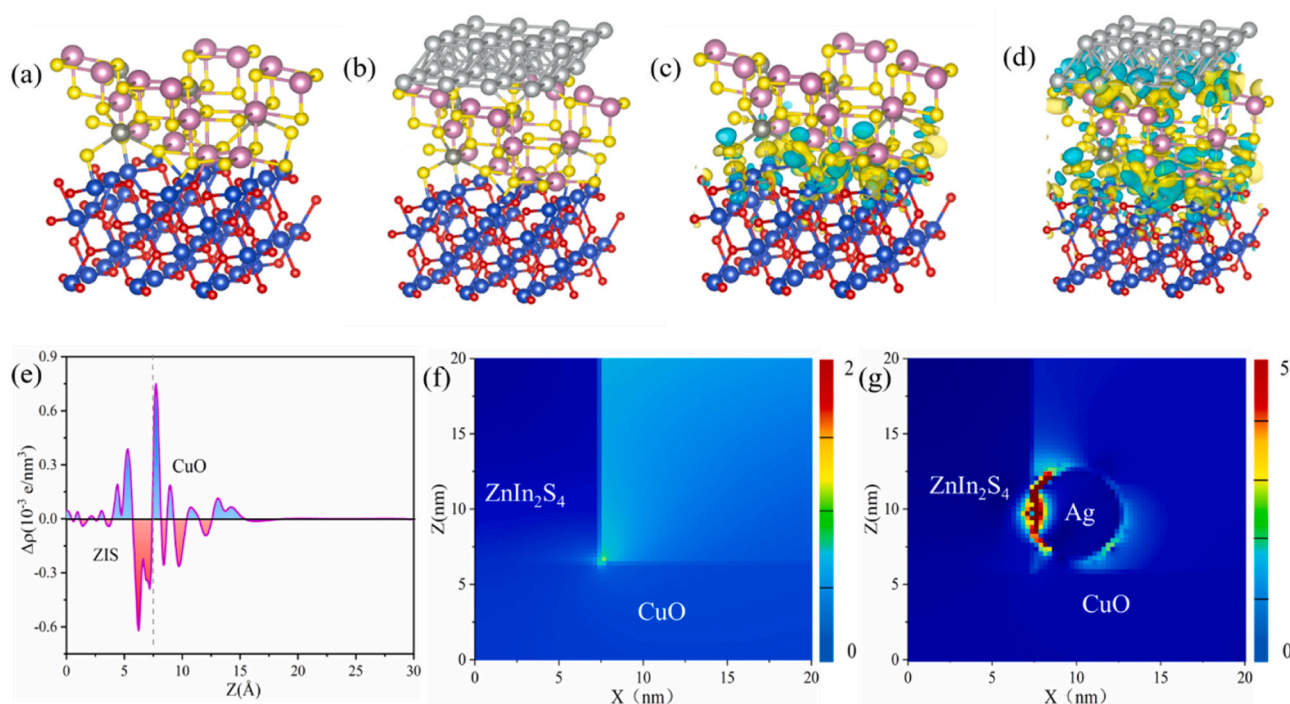


Fig. 10. The crystal structure of the (a) CZ and (a) ACZ. The charge density difference of the (c) CZ and (d) ACZ. (e) Planar average charge density difference. The FDTD simulated electric field distributions calculated at the cross-sections of (f) 15-CZ and (g) 15-ACZ with excited light-wavelength at 420 nm.

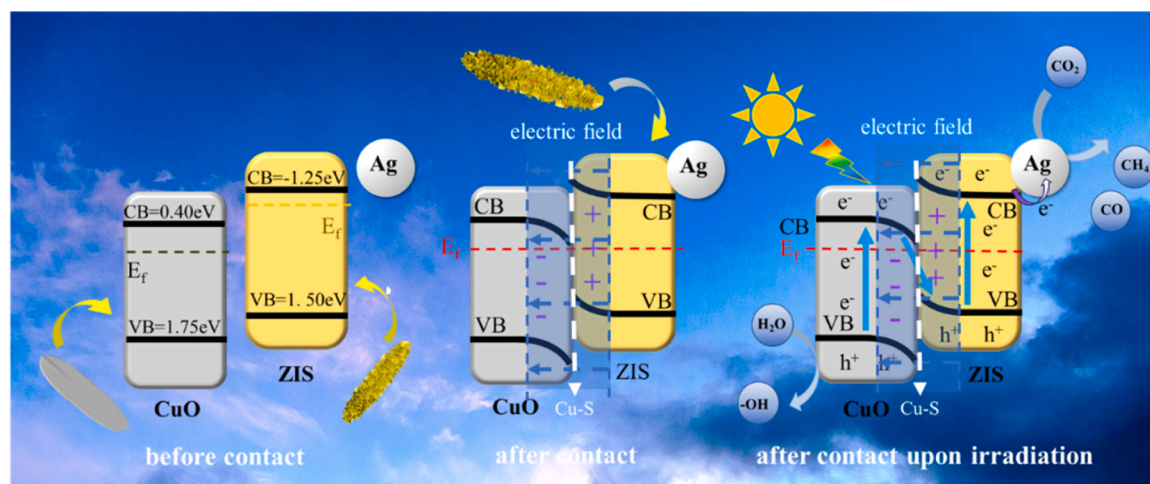


Fig. 11. Photocatalytic mechanism of ACZ.

characterized were CO and CH₄. In particular, the results of catalyst performance tests showed that 15-ACZ exhibited optimal photocatalytic activity under light irradiation, and the CO and CH₄ yields were 16.9 $\mu\text{mol g}^{-1} \text{h}^{-1}$ and 54.4 $\mu\text{mol g}^{-1} \text{h}^{-1}$, wherein, the selectivity of CH₄ product can reach 92.8%. This efficient conversion can be attributed to the IEF constructed by the S-scheme heterojunction and the Cu-S covalent bond formed by the tight junctions of the two monomers facilitating the directional separation of the photoexcited charges. In addition, Ag acts as a cocatalyst to capture electrons in the CB of ZIS, while using the LSPR effect to enhance light absorption and provide more hot electrons for the reaction. Therefore, well designed Ag/CuO@ZnIn₂S₄ plasmonic S-scheme heterojunction can be used as a rational and effective structural composite photocatalyst for highly active and selective methanation of CO₂. This work provides potential guidance for introducing covalent bonds into the S-scheme heterojunction photocatalysts with plasma effects to achieve highly selective

photoconversion of CO₂.

CRediT authorship contribution statement

Yining Zhang: Investigation, Writing – original draft, Methodology. **Jinze Li:** Investigation, Data curation, Formal analysis. **Weiqliang Zhou:** Investigation, Writing – review & editing. **Xin Liu:** Supervision, Methodology. **Xianghai Song:** Methodology. **Songtao Chen:** Validation. **Huiqin Wang:** Supervision, Writing – review & editing. **Pengwei Huo:** Supervision, Conceptualization, Writing – review & editing, Funding acquisition.

Declaration of Competing Interest

The authors declare that they have no known competing financial interests or personal relationships that could have appeared to influence

the work reported in this paper.

Data availability

No data was used for the research described in the article.

Acknowledgments

This work has been financially supported by the National Natural Science Foundation of China (Nos. 22078131 and 22108102). The Science and Technology Planning Social Development Project of Zhenjiang City (No. SH2021013). The Natural Science Foundation of the Jiangsu Higher Education Institutions of China (No. 21KJB430036). The Jiangsu Provincial Funds for Young Scholars (No. BK20210782). The China Postdoctoral Science Foundation (No. 2023TQ0381).

Appendix A. Supporting information

Supplementary data associated with this article can be found in the online version at doi:10.1016/j.apcatb.2023.123449.

References

- [1] E. Gong, S. Ali, C. Hiragond, H. Kim, N. Powar, D. Kim, H. Kim, S. In, Solar fuels: research and development strategies to accelerate photocatalytic CO₂ conversion into hydrocarbon fuels, *Energy Environ. Sci.* 15 (2022) 880–937.
- [2] Y. Ma, X. Yi, S. Wang, T. Li, B. Tan, C. Chen, T. Majima, E. Wacławik, H. Zhu, J. Wang, Selective photocatalytic CO₂ reduction in aerobic environment by microporous Pd-porphyrin-based polymers coated hollow TiO₂, *Nat. Commun.* 13 (2022) 1400.
- [3] X. Shi, Y. Huang, Y. Bo, D. Duan, Z. Wang, J. Cao, G. Zhu, W.K. Ho, L. Wang, T. Huang, Y. Xiong, Highly selective photocatalytic CO₂ methanation with water vapor on single-atom platinum-decorated defective carbon nitride, *Angew. Chem. Int. Ed. Engl.* 61 (2022), e202203063.
- [4] J. Zhou, J. Li, L. Kan, L. Zhang, Q. Huang, Y. Yan, Y. Chen, J. Liu, S. Li, Y. Lan, Linking oxidative and reductive clusters to prepare crystalline porous catalysts for photocatalytic CO₂ reduction with H₂O, *Nat. Commun.* 13 (2022) 4681.
- [5] X. Jiang, J. Huang, Z. Bi, W.J. Ni, G. Gursadyan, Y. Zhu, Z. Zhang, Plasmonic active “hot spots”-confined photocatalytic CO₂ reduction with high selectivity for CH₄ production, *Adv. Mater.* 34 (2022), e2109330.
- [6] S. Liu, J. Wang, J. Yu, ZIF-8 derived bimodal carbon modified ZnO photocatalysts with enhanced photocatalytic CO₂ reduction performance, *RSC Adv.* 6 (2016) 59998–60006.
- [7] J. Wang, S. Lin, N. Tian, T. Ma, Y. Zhang, H. Huang, Nanostructured metal sulfides: classification, modification strategy, and solar-driven CO₂ reduction application, *Adv. Funct. Mater.* 31 (2020) 2008008.
- [8] G. Tang, J. Li, Y. Lu, T. Song, S. Yin, G. Mao, B. Long, A. Ali, G. Deng, Donor-acceptor organic polymer with sulfur bridge for superior photocatalytic CO₂ reduction to CH₄ under visible light illumination, *Chem. Eng. J.* 451 (2023), 138744.
- [9] X. Lin, S. Xia, L. Zhang, Y. Zhang, S. Sun, Y. Chen, S. Chen, B. Ding, J. Yu, J. Yan, Fabrication of flexible mesoporous black Nb₂O₅ nanofiber films for visible-light-driven photocatalytic CO₂ reduction into CH₄, *Adv. Mater.* 34 (2022), e2200756.
- [10] N. Sun, Y. Zhu, M. Li, Zhang, J. Qin, Y. Li, C. Wang, Thermal coupled photocatalysis over Pt/g-C₃N₄ for selectively reducing CO₂ to CH₄ via the cooperation of the electronic metal-support interaction effect and the oxidation state of Pt, *Appl. Catal. B Environ.* 298 (2021), 120565.
- [11] D. Li, C. Zhou, X. Xie, D. Chen, Y. Zhou, X. Shi, D. Jiang, M. Chen, W. Shi, Steering multistep charge transfer for highly selectively photocatalytic reduction of CO₂ into CH₄ over Pd/Cu₂O/TiO₂ ternary hybrid, *Sol. RRL* 5 (2021) 2000813.
- [12] S. Si, H. Shou, Y. Mao, X. Bao, G. Zhai, K. Song, Z. Wang, P. Wang, Y. Liu, Z. Zheng, Y. Dai, L. Song, B. Huang, H. Cheng, Low-coordination single Au atoms on ultrathin ZnIn₂S₄ nanosheets for selective photocatalytic CO₂ reduction towards CH₄, *Angew. Chem. Int. Ed. Engl.* 61 (2022), e202209446.
- [13] Y. Zhong, M. Li, X. Luan, F. Gao, H. Wu, J. Zi, Z. Lian, Ultrathin ZnIn₂S₄/ZnSe heteronanoseeds with modulated S-scheme enable high efficiency of visible-light-responsive photocatalytic hydrogen evolution, *Appl. Catal. B Environ.* 335 (2023), 122859.
- [14] H. Zhang, Z. Wang, J. Zhang, K. Dai, Metal-sulfide-based heterojunction photocatalysts: principles, impact, applications, and in-situ characterization, *Chin. J. Catal.* 49 (2023) 42–67.
- [15] M. Sheng, C. Gan, Y. Li, Z. Hu, Q. Zhou, L. Qin, J. Ren, H. Jiang, Photocatalytic C-O activation and biomass derived polymer precursor production with CO₂ over redox centers spatially separated Sv-ZnIn₂S₄/BiVO₄, *Appl. Catal. B Environ.* 339 (2023), 123138.
- [16] Y. Song, Y. Wang, C. Hu, C. Ye, Z. Qian, Y. Zhao, W. Cai, Facet engineering-induced construction of Ni₂P/ZnIn₂S₄ heterostructures for boosted photocatalytic CO₂ reduction, *ACS Appl. Mater. Interfaces* 15 (2023) 30199–30211.
- [17] Y. Ding, Y. Chen, Z. Guan, Y. Zhao, J. Lin, Y. Jiao, G. Tian, Hierarchical CuS@ZnIn₂S₄ hollow double-shelled p-n heterojunction octahedra decorated with fullerene C₆₀ for remarkable selectivity and activity of CO₂ photoreduction into CH₄, *ACS Appl. Mater. Interfaces* 14 (2022) 7888–7899.
- [18] Q. Xu, L. Zhang, B. Cheng, J. Fan, J. Yu, S-Scheme heterojunction photocatalyst, *Chem* 6 (2020) 1543–1559.
- [19] B. Dai, Y. Li, J. Xu, C. Sun, S. Li, W. Zhao, Photocatalytic oxidation of tetracycline, reduction of hexavalent chromium and hydrogen evolution by Cu₂O/g-C₃N₄ S-scheme photocatalyst: performance and mechanism insight, *Appl. Surf. Sci.* 592 (2022), 153309.
- [20] F. Li, X. Yue, Y. Liao, L. Qiao, K. Lv, Q. Xiang, Understanding the unique S-scheme charge migration in triazine/heptazine crystalline carbon nitride homojunction, *Nat. Commun.* 14 (2023) 3901.
- [21] L. Wang, B. Cheng, L. Zhang, J. Yu, In situ irradiated XPS investigation on S-scheme TiO₂@ZnIn₂S₄ photocatalyst for efficient photocatalytic CO₂ reduction, *Small* 17 (2021), e2103447.
- [22] S. Qin, F. Xin, Y. Liu, X. Yin, W. Ma, Photocatalytic reduction of CO₂ in methanol to methyl formate over CuO-TiO₂ composite catalysts, *J. Colloid Interface Sci.* 356 (2011) 257–261.
- [23] Y. Song, C. Ye, X. Yu, J. Tang, Y. Zhao, W. Cai, Electron-induced enhanced interfacial interaction of the CuO/BiOCl heterostructure for boosted CO₂ photoreduction performance under simulated sunlight, *Appl. Surf. Sci.* 583 (2022), 152463.
- [24] T. Han, H. Shi, Y. Chen, Facet-dependent CuO/{010}BiVO₄ S-scheme photocatalyst enhanced peroxymonosulfate activation for efficient norfloxacin removal, *J. Mater. Sci. Technol.* (2023) 2–40.
- [25] W. Soontornchaiyakul, S. Yoshino, T. Kanazawa, R. Haruki, D. Fan, S. Nozawa, Y. Yamaguchi, A. Kudo, CH₄ Synthesis from CO₂ and H₂O of an electron source over Rh-Ru cocatalysts loaded on NaTaO₃:Sr photocatalysts, *J. Am. Chem. Soc.* (2023).
- [26] C.B. Hiragond, S. Biswas, N.S. Powar, J. Lee, E. Gong, H. Kim, H.S. Kim, J.W. Jung, C.H. Cho, B.M. Wong, S.I. In, Surface-modified Ag@Ru-P₂₅ for photocatalytic CO₂ conversion with high selectivity over CH₄ formation at the solid–gas interface, *Carbon Energy* (2023), e386.
- [27] Y. Fu, Y. Xu, Y. Mao, M. Tan, Q. He, H. Mao, H. Du, D. Hao, Q. Wang, Multi-functional Ag/Ag₃PO₄/AgPMo with S-scheme heterojunction for boosted photocatalytic performance, *Sep. Purif. Technol.* 317 (2023), 123922.
- [28] Q. Li, W. Zhao, Z. Zhai, K. Ren, T. Wang, H. Guan, H. Shi, 2D/2D Bi₂MoO₆/g-C₃N₄ S-scheme heterojunction photocatalyst with enhanced visible-light activity by Au loading, *J. Mater. Sci. Technol.* 56 (2020) 216–226.
- [29] M. Zhang, X. Wang, X. Qi, H. Guo, L. Liu, Q. Zhao, W. Cui, Effect of Ag cocatalyst on highly selective photocatalytic CO₂ reduction to HCOOH over CuO/Ag/Uio-66 Z-scheme heterojunction, *J. Catal.* 413 (2022) 31–47.
- [30] X. Li, H. Jiang, C. Ma, Z. Zhu, X. Song, H. Wang, P. Huo, X. Li, Local surface plasma resonance effect enhanced Z-scheme ZnO/Au/g-C₃N₄ film photocatalyst for reduction of CO₂ to CO, *Appl. Catal. B Environ.* 283 (2021), 119638.
- [31] A. Raza, H. Shen, A. Haidry, Novel Cu₂ZnSnS₄/Pt/g-C₃N₄ heterojunction photocatalyst with straddling band configuration for enhanced solar to fuel conversion, *Appl. Catal. B Environ.* 277 (2020), 119239.
- [32] Z. Jiang, Q. Chen, Q. Zheng, R. Shen, P. Zhang, X. Li, Constructing 1D/2D schottky-based heterojunctions between Mn_{0.2}Cd_{0.8}S nanorods and Ti₃C₂ nanosheets for boosted photocatalytic H₂ evolution, *Acta Phys. Chim. Sin.* 0 (2020), 2010059–2010050.
- [33] Y. Zhang, M. Xu, W. Zhou, X. Song, X. Liu, J. Zhang, S. Chen, P. Huo, Fabricated ZnO@ZnIn₂S₄ S-scheme heterojunction photocatalyst for enhanced electron-transfer and CO₂ reduction, *J. Colloid Interface Sci.* 650 (2023) 1762–1772.
- [34] X. Li, W. He, C. Li, B. Song, S. Liu, Synergetic surface modulation of ZnO/Pt-ZIF-8 hybrid nanorods for enhanced photocatalytic CO₂ valorization, *Appl. Catal. B Environ.* 287 (2021), 119934.
- [35] Y. Cui, C. Yang, H. Lin, S. Rui, D. Yao, Y. Liao, C. Zhang, Y. Fang, X. Wang, Z. Zhong, Y. Song, G. Wang, L. Zhuang, Z. Li, Amorphous NXC coating promotes electrochemical CO₂ deep reduction to hydrocarbons over Ag nanocatalysts, *ACS Catal.* (2022) 169–178.
- [36] M. Li, W. Qi, J. Yu, L. Shen, X. Yang, S. Liu, M. Yang, Ultrathin ZnIn₂S₄ nanosheets-supported metallic Ni₃FeN for photocatalytic coupled selective alcohol oxidation and H₂ evolution, *Chin. J. Struct. Chem.* 41 (2022) 221015–221024.
- [37] H. He, Z. Wang, K. Dai, S.W. Li, J.F. Zhang, LSPR-enhanced carbon-coated In₂O₃/W₁₈O₄₉ S-scheme heterojunction for efficient CO₂ photoreduction, *Chin. J. Catal.* 48 (2023) 267–278.
- [38] Y. Zhang, Y. Wu, L. Wan, H. Ding, H. Li, X. Wang, W. Zhang, Hollow core-shell Co₉S₈@ZnIn₂S₄/CdS nanoreactor for efficient photothermal effect and CO₂ photoreduction, *Appl. Catal. B Environ.* 311 (2022), 121255.
- [39] L. Xiao, C. Yuan, P. Chen, Y. Liu, J. Sheng, S. Zhang, F. Dong, Y. Sun, Cu–S bonds as an atomic-level transfer channel to achieve photocatalytic CO₂ reduction to CO on Cu-substituted ZnIn₂S₄, *ACS Sustain. Chem. Eng.* 10 (2022) 11902–11912.
- [40] W. Xu, W. Gao, L. Meng, W. Tian, L. Li, Incorporation of sulfate anions and sulfur vacancies in ZnIn₂S₄ photoanode for enhanced photoelectrochemical water splitting, *Adv. Energy Mater.* 11 (2021) 2101181.
- [41] Y. Wang, M. Liu, C. Wu, J. Gao, M. Li, Z. Xing, Z. Li, W. Zhou, Hollow nanoboxes Cu₂-xS@ZnIn₂S₄ core-shell S-scheme heterojunction with broad-spectrum response and enhanced photothermal-photocatalytic performance, *Small* 18 (2022), e2202544.
- [42] G. Yang, P. Qiu, J. Xiong, X. Zhu, G. Cheng, Facilely anchoring Cu₂O nanoparticles on mesoporous TiO₂ nanorods for enhanced photocatalytic CO₂ reduction through efficient charge transfer, *Chin. Chem. Lett.* 33 (2022) 3709–3712.

- [43] A. Boonstra, C.A. Mutsaers, Photoadsorption of oxygen and the number of hydroxyl groups, *J. Phys. Chem.* 79 (16) (1974) 1694–1698.
- [44] J. Bai, R. Shen, Z. Jiang, P. Zhang, Y. Li, X. Li, Integration of 2D layered CdS/WO₃ S-scheme heterojunctions and metallic Ti₃C₂ MXene-based Ohmic junctions for effective photocatalytic H₂ generation, *Chin. J. Catal.* 43 (2022) 359–369.
- [45] J. Zou, G. Liao, J. Jiang, Z. Xiong, S. Bai, H. Wang, P. Wu, P. Zhang, X. Li, In-situ construction of sulfur-doped g-C₃N₄/defective g-C₃N₄ isotype step-scheme heterojunction for boosting photocatalytic H₂ evolution, *Chin. J. Struct. Chem.* 41 (1) (2022) 2201025–2201033.
- [46] J. Li, Y. Li, X. Wang, Z. Yang, G. Zhang, Atomically dispersed Fe sites on TiO₂ for boosting photocatalytic CO₂ reduction: enhanced catalytic activity, DFT calculations and mechanistic insight, *Chin. J. Catal.* 51 (2023) 145–156.
- [47] D. Zhang, R. Zhang, J. Liu, X. Pu, P. Cai, 3D/2D ZnIn₂S₄/BiFeO₃ as S-scheme heterojunction photocatalyst for boosted visible-light hydrogen evolution, *J. Am. Ceram. Soc.* 106 (2023) 4785–4793.
- [48] M. Zhang, X. Wang, X. Qi, H. Guo, L. Liu, Q. Zhao, W. Cui, Effect of Ag cocatalyst on highly selective photocatalytic CO₂ reduction to HCOOH over CuO/Ag/Uio-66 Z-scheme heterojunction, *J. Catal.* 413 (2022) 31–47.
- [49] X. Wang, Z. Jiang, H. Chen, K. Wang, X. Wang, Photocatalytic CO₂ reduction with water vapor to CO and CH₄ in a recirculation reactor by Ag-Cu₂O/TiO₂ Z-scheme heterostructures, *J. Alloy. Compd.* 896 (2022), 163030.
- [50] J. Wang, X. Qiao, W. Shi, H. Gao, L.C. Guo, Enhanced photothermal selective conversion of CO₂ to CH₄ in water vapor over rod-like Cu and N Co-doped TiO₂, *Chin. J. Struct. Chem.* 41 (2022) 2212033–2212042.
- [51] B. Su, M. Zheng, W. Lin, X.F. Lu, D. Luan, S. Wang, X.W. Lou, S-scheme Co₉S₈@Cd_{0.8}Zn_{0.2}S-DETA hierarchical nanocages bearing organic CO₂ activators for photocatalytic syngas production, *Adv. Energy Mater.* 13 (2023) 2203290.
- [52] G. Sun, Z. Tai, F. Li, Q. Ye, T. Wang, Z. Fang, L. Jia, W. Liu, H. Wang, Construction of ZnIn₂S₄/CdS/PdS S-scheme heterostructure for efficient photocatalytic H₂ production, *Small* (2023), e2207758.
- [53] Z. Tang, C. Wang, W. He, Y. Wei, Z. Zhao, J. Liu, The Z-scheme g-C₃N₄/3DOM-WO₃ photocatalysts with enhanced activity for CO₂ photoreduction into CO, *Chin. Chem. Lett.* 33 (2022) 939–942.
- [54] L. Jiang, Y. Li, X. Wu, G. Zhang, Rich oxygen vacancies mediated bismuth oxysulfide crystals towards photocatalytic CO₂-to-CH₄ conversion, *Sci. China Mater.* 64 (2021) 2230–2241.
- [55] H. Che, X. Gao, J. Chen, J. Hou, Y. Ao, P. Wang, Iodide-induced fragmentation of polymerized hydrophilic carbon nitride for high-performance quasi-homogeneous photocatalytic H₂O₂ production, *Angew. Chem. Int. Ed. Engl.* 60 (2021) 25546–25550.
- [56] Y. Wu, J. Chen, H. Che, X. Gao, Y. Ao, P. Wang, Boosting 2e⁻ oxygen reduction reaction in garland carbon nitride with carbon defects for high-efficient photocatalysis-self-Fenton degradation of 2,4-dichlorophenol, *Appl. Catal. B Environ.* 307 (2022), 121185.
- [57] Z. Lei, X. Cao, J. Fan, X. Hu, J. Hu, N. Li, T. Sun, E. Liu, Efficient photocatalytic H₂ generation over In_{2.77}S₄/NiS₂/g-C₃N₄ S-scheme heterojunction using NiS₂ as electron-bridge, *Chem. Eng. J.* 457 (2023), 141249.
- [58] Z. Zhao, Z. Wang, J. Zhang, C. Shao, K. Dai, K. Fan, C. Liang, Interfacial chemical bond and oxygen vacancy-enhanced In₂O₃/CdSe-DETA S-scheme heterojunction for photocatalytic CO₂ conversion, *Adv. Funct. Mater.* 33 (2023) 2214470.
- [59] H. An, Z. Lv, K. Zhang, C. Deng, H. Wang, Z. Xu, M. Wang, Z. Yin, Plasmonic coupling enhancement of core-shell Au@Pt assemblies on ZnIn₂S₄ nanosheets towards photocatalytic H₂ production, *Appl. Surf. Sci.* 536 (2021), 147934.
- [60] X. Wang, Z. Wang, Y. Li, J. Wang, G. Zhang, Efficient photocatalytic CO₂ conversion over 2D/2D Ni-doped CsPbBr₃/Bi₃O₄Br Z-scheme heterojunction: Critical role of Ni doping, boosted charge separation and mechanism study, *Appl. Catal. B Environ.* 319 (2022), 121895.
- [61] X. Zhao, M. Xu, X. Song, W. Zhou, X. Liu, P. Huo, 3D Fe-MOF embedded into 2D thin layer carbon nitride to construct 3D/2D S-scheme heterojunction for enhanced photoreduction of CO₂, *Chin. J. Catal.* 43 (2022) 2625–2636.
- [62] J. Li, X. Pei, Z. Wang, Y. Li, G. Zhang, Boosted charge transfer and selective photocatalytic CO₂ reduction to CH₄ over sulfur-doped K_{0.475}WO₃ nanorods under visible light: performance and mechanism insight, *Appl. Surf. Sci.* 605 (2022), 154632.
- [63] C. Luo, Q. Long, B. Cheng, B.C. Zhu, L.X. Wang, A DFT study on S-scheme heterojunction consisting of Pt single atom loaded g-C₃N₄ and BiOCl for photocatalytic CO₂ reduction, *Acta Phys. Chim. Sin.* 39 (2023) 2212026.
- [64] Z. Zhu, H. Huang, L. Liu, F. Chen, Na Tian, Y. Zhang, H. Yu, Chemically bonded α-Fe₂O₃/Bi₄MO₈Cl dot-on-plate Z-scheme junction with strong internal electric field for selective photo-oxidation of aromatic alcohols, *Angew. Chem.* 60 (2022), e202203519.
- [65] Z. Xu, W. Yue, C. Li, L. Wang, Y. Xu, Z. Ye, J. Zhang, Rational synthesis of Au-CdS composite photocatalysts for broad-spectrum photocatalytic hydrogen evolution, *ACS Nano* 17 (2023) 11655–11664.
- [66] X. Yu, X. Liu, B. Wang, Q. Meng, S. Sun, Y. Tang, K. Zhao, An LSPR-based "push-pull" synergetic effect for the enhanced photocatalytic performance of a gold nanorod@cuprous oxide-gold nanoparticle ternary composite, *Nanoscale* 12 (2020) 1912–1920.
- [67] J. Zou, G. Liao, J. Jiang, Z.G. Xiong, S. Bai, H. Wang, P. Wu, P. Zhang, X. Li, In-situ construction of sulfur-doped g-C₃N₄/defective g-C₃N₄ iso-type step-scheme heterojunction for boosting photocatalytic H₂ evolution, *Chin. J. Struct. Chem.* 41 (2022) 2201025–2201033.
- [68] T. Sun, C. Li, Y. Bao, J. Fan, E. Liu, S-scheme MnCo₂S₄/g-C₃N₄ heterojunction photocatalyst for H₂ production, *Acta Phys. Chim. Sin.* 39 (2023) 2212009.
- [69] Z. Zan, X. Li, X. Gao, J. Huang, Y. Luo, L. Han, 0D/2D carbon nitride quantum dots (CNQDs)/BiOBr S-scheme heterojunction for robust photocatalytic degradation and H₂O₂ production, *Acta Phys. Chim. Sin.* 39 (2023) 2209016.